TU Delft

Delft University of Technology

Document Version
Final published version

Licence
Dutch Copyright Act (Article 25fa)

Citation (APA)
Zaier, R., Hattem, A. V., de Waal, B. N., Konings, R. J. M., Smith, A. L., Zeller, P., & Guéneau, C. (2026). A thermodynamic model of the Cs-Pb system. *Calphad: Computer Coupling of Phase Diagrams and Thermochemistry*, *93*, Article 102941. https://doi.org/10.1016/j.calphad.2026.102941

Important note
To cite this publication, please use the final published version (if applicable).
Please check the document version above.

Copyright
In case the licence states “Dutch Copyright Act (Article 25fa)”, this publication was made available Green Open Access via the TU Delft Institutional Repository pursuant to Dutch Copyright Act (Article 25fa, the Taverne amendment). This provision does not affect copyright ownership.
Unless copyright is transferred by contract or statute, it remains with the copyright holder.

Sharing and reuse
Other than for strictly personal use, it is not permitted to download, forward or distribute the text or part of it, without the consent of the author(s) and/or copyright holder(s), unless the work is under an open content license such as Creative Commons.

Takedown policy
Please contact us and provide details if you believe this document breaches copyrights.
We will remove access to the work immediately and investigate your claim.

This work is downloaded from Delft University of Technology.

CALPHAD: Computer Coupling of Phase Diagrams and Thermochemistry 93 (2026) 102941

Contents lists available at ScienceDirect

Calphad

journal homepage: www.elsevier.com/locate/calphad

A thermodynamic model of the Cs-Pb system

Rania Zaier [a,*], Andries van Hattem [b], Brandon N. de Waal [b], Rudy J.M. Konings [b], Anna L. Smith [b], Philippe Zeller [a], Christine Guéneau [a,**]

[a] Université Paris-Saclay, CEA, Service de Recherche en Corrosion et Comportement des Matériaux, 91191, Gif-sur-Yvette, France
[b] Faculty of Applied Sciences, Radiation Science & Technology Department, Delft University of Technology, Mekelweg 15, Delft, 2629JB, the Netherlands

ARTICLE INFO

Keywords:
Cs-Pb
CALPHAD
DFT calculations
Lead-cooled fast reactor
Perovskite-based photovoltaics
Short-range ordering in liquid

ABSTRACT

A comprehensive thermodynamic assessment of the Cs-Pb system was performed with the CALPHAD method using the experimental thermodynamic and phase diagram data available in literature supplemented by density functional theory (DFT) calculations. The exact nature of the stable compounds in the phase diagrams reported in the literature is uncertain, except for CsPb and Cs_4Pb_9 whose crystalline structures are well known. Therefore, DFT calculations were performed to calculate the energy of formation at 0 K of different possible compounds with various crystalline structures. The enthalpies of formation of the compounds CsPb, Cs_4Pb_9, and $CsPb_4$, found to be the stable ones by DFT, were then used in the CALPHAD model. The result of this process has enabled the development of a more refined phase diagram comparing to experimental ones, providing more comprehensive insights into the phase equilibria in this system. Moreover, the CALPHAD model succeeded in describing the peculiar behavior of the heat capacity of the liquid phase, by using an ionic two-sublattice model $(Cs^{+1})_P(Pb^{-1}, Va,Pb)_Q$ which takes into account the short-range ordering taking place at the equimolar composition CsPb, related to the formation of clusters Cs_4Pb_4, modelled as (Cs^{+1}) (Pb^{-1}). The model allows for the prediction of important thermodynamic properties, which are of interest for a range of applications, including lead-cooled fast reactors and perovskite-based photovoltaics.

1. Introduction

The Cs-Pb system has received mainly academic interest in the past, in particular in view of its interesting physical properties in the liquid state. The system shows a very high resistivity at $x = 0.5$ which was explained by the formation of Pb_4 tetrahedra in the liquid [1]. The strong decrease of the resistivity with temperature was moreover interpreted to be caused by disintegration of the tetrahedra at higher temperatures. The molar volume shows a strong negative excess deviation from ideal volumetric behavior at $x = 0.5$ as well, which was attributed to Pb_4 tetrahedra (Zintl polyanions) surrounded by four alkali cations [2]. The Cs-Pb system also has relevance as binary sub-system in multi-element systems with Cs and Pb. Currently two of these multi-element systems are in the focus of research, and form the basis for the current work: (i) The systems Cs-Mo-Pb-O and Cs-Pb-I are of high relevance for the safety assessment of lead-cooled fast reactors (LFR) to assess the chemical interaction of fission products (Cs, Mo, I) in the lead coolant. (ii) Inorganic alkali halide perovskite ($CsPbX_3$, X = I, Br, Cl) are promising optical materials with application in photovoltaic and light-emitting devices [3,4].

LFRs use either liquid lead (Pb) or a liquid lead-bismuth eutectic mixture (LBE) as coolant material. Historically, LBE especially has been used as coolant in nuclear-powered submarines. More recently, the Generation IV International Forum identified LFRs as one of six promising technologies for the next generation of nuclear fission reactors. They have gained attention as fast neutron reactors for electricity production as well as being dedicated “nuclear burners” for the consumption of reprocessed plutonium and minor actinides (MAs), e.g. americium, curium, and neptunium. Additionally, Pb and LBE provide considerable safety benefits characteristics compared to the other considered metal coolant for fast reactors, namely sodium, such as inertness towards water and air, and high boiling points, effectively eliminating the risk of coolant boiling. Currently, a 300 MWe LFR (BREST) is under construction in Russia, with several other LFRs in the design phase, including MYRRHA in Belgium.

In Europe, the reference fuel for LFRs is a mixed oxide $(U,Pu)O_2$ fuel,

* Corresponding author.
** Corresponding author.
E-mail addresses: rania.zaier02@gmail.com (R. Zaier), christine.gueneau@cea.fr (C. Guéneau).

https://doi.org/10.1016/j.calphad.2026.102941
Received 11 December 2025; Received in revised form 2 March 2026; Accepted 10 March 2026
Available online 19 March 2026
0364-5916/© 2026 Published by Elsevier Ltd.

with around 20-30 % Pu. At a burn-up higher than 7-8 % FIMA (fissions per initial metal atom), a Joint Oxyde Gaine (JOG) is expected to be formed between the fuel rod and the cladding as in Sodium cooled Fast Reactors [5]. This JOG layer forms due to the high temperatures and thermal gradients in the fuel pellet, leading to migration of the volatile fission products towards the cooler cladding. The JOG consists of molybdenum (Mo) and major volatile fission products, such as cesium (Cs) and iodine (I). In the event of a cladding failure, these fission products will be released into the coolant, the consequences of which need to be assessed carefully. Furthermore, Cs is produced in trace amounts as spallation product in the Pb target of an Accelerator Driven System (ADS), which is a specific concept of a burner LFRs. Overall, Cs (radioactive isotopes ^{134}Cs, ^{135}Cs and ^{137}Cs) is of particular concern in safety analyses due to its high volatility increasing the likelihood of it permeating into the coolant in case of a clad breach. However, several sources cite a high retention capacity of Cs in Pb and LBE [6–8].

In order to enable the design field of perovskite solar cells (PSCs) development, the cesium lead halide perovskites ($CsPbX_3$, X = I, Br) have demonstrated considerable optoelectronic properties, including large absorption coefficients and efficient long carrier diffusion lengths, making them promising materials [9,10]. These significant features have advanced PSCs to the rank of the most innovative photovoltaic technologies, with power conversion rates (PCEs) exceeding 26% in only ten years of development [11], thus approaching the performance of traditional crystalline silicon solar cells. Their tunable band gap and the ease of economic application of perovskite materials make them prime candidates for adaptable and flexible photovoltaic systems. However, despite these advantages, several challenges remain that limit the practical use of $CsPbX_3$ perovskites, with stability issues being the most significant. Although inorganic chlorine-based perovskites ($CsPbCl_3$) exhibit higher stability, they are less favored due to their wide band gaps (>3eV) [12]. The stability of perovskite materials is problematic in the presence of moisture, oxygen, and UV radiation, resulting thereby in film degradation [13]. In addition, ion movement, surface mixing, and phase separation in mixed halide systems can reduce device performance and quality. Research is being conducted on the composition, surface treatment, and interface design of $CsPbX_3$ PSCs to improve their stability and performance.

Understanding the stability of the perovskite layer is crucial for device performance and durability. Thus, before synthesizing lead halide perovskites, it is necessary to first acquire a better knowledge of these materials, including the equilibrium thermodynamic properties of the relevant phases. In this context, we aim to develop a global thermodynamic model for the Cs-Pb-Br-I system. The CALPHAD methodology consists in first elaborating accurate thermodynamic descriptions of the binary subsystems and then extending the model to more complex ternary and quaternary systems.

This work is devoted to the Cs-Pb binary subsystem, for which we study the phase thermodynamic stability and phase equilibria. We first collect and examine the available experimental data to identify gaps in knowledge and inconsistencies. First-principles calculations based on Density Functional Theory (DFT) are used to complete the missing experimental data for the enthalpies of formation of the solid compounds. Finally, we use the full dataset to conduct the thermodynamic assessment and construct a reliable thermodynamic model for the Cs-Pb system. A comparison between the calculated and experimental data is presented. Since the literature study revealed several gaps in the available experimental data, some recommendations for future experiments are given at the end of the article.

2. Literature review of the system Cs-Pb

2.1. Phase diagram data

The Cs-Pb system was studied several times in the previous century, and gained renewed interest in recent years. Two independent experimental phase diagrams of the Cs-Pb binary system have been published. Meijer et al. [14] conducted a study on the resistivity of liquid Cs-Pb alloys as a function of temperature and composition in 1986, yielding the phase diagram given in Figure S.1. In a large part of literature, this has been regarded as the only available phase diagram, while an independently established phase diagram by differential thermal analysis (DTA) was already published by Zusman in 1976 [15], shown in Figure S2.

Both phase diagrams propose four intermetallic compounds, namely CsPb and three others with approximate stoichiometries Cs_4Pb_5, $CsPb_2$ and $CsPb_3$.

Significant discrepancies are observed between the two published phase diagrams. The melting temperature of CsPb reported by Zusman [15] (926 K) is 33 K higher than that measured by Meijer et al. [14] (893 K). The experimental liquidus reported by Zusman [15] appears noticeably lower on both Cs-rich and Pb-rich sides. Also, Meijer et al. [14] represented Cs_5Pb_4 with a dashed line, indicating uncertainty regarding the existence of this transition. Moreover, the transition at x (Pb) = 0.75 corresponding to the peritectic $CsPb_3 = CsPb_2 + L$ occurred at temperature approximately 173 K higher in Zusman's [15] (791 K) phase diagram compared to that of Meijer et al. [14] (618 K).

From a crystallographic point of view, only two structures in the Cs-Pb binary system have been investigated experimentally thoroughly: CsPb (Cs_4Pb_4) and Cs_4Pb_9 [16,17], the latter not identified in the phase diagram studies. The reported space groups and lattice parameters are summarized in Table 1.

These discrepancies regarding the existence of the compounds between the experimental phase diagrams and crystallographic data require a critical evaluation of the available experimental data to see whether a consistent picture between phase diagram determinations and crystallographic data can be obtained.

- The existence of CsPb, including the α-CsPb → β-CsPb transition as evidenced from the enthalpy increment measurements from Refs. [18,19], is clearly established.
- Continuing from crystallography and assuming stoichiometric compounds only, the compound $CsPb_2$ (x(Pb) = 0.667) can be reinterpreted as Cs_4Pb_9 (x(Pb) = 0.692), although the traces of Pb found in Cs_4Pb_9 syntheses and the Differential Scanning Calorimetry (DSC) data could be used as counterargument, see Fig. 2 (optimized phase diagram with all data) where phase transitions were observed at x (Pb) = 0.67. Two other compounds were proposed by the phase diagram studies: Cs_4Pb_5 and $CsPb_3$. Cs_4Pb_5 was drawn as a dashed line by Meijer et al. in the phase diagram, and neither Meijer et al. nor Zusman included the high temperature phase transition of CsPb. This makes the existence of Cs_4Pb_5 rather unlikely and we thus do not include it in the thermodynamic model. $CsPb_3$ was proposed by both authors, but the discrepancy in peritectic decomposition temperature is large: Zusman gave 791 K, while Meijer et al. reported 618 K. This structure has not been found elsewhere in other literature, and DFT calculations have not yet identified a stable structure at this composition [20]. The Cs-Pb system has also been studied in the frame of the OQMD project using DFT [21]. Alongside the CsPb and Cs_4Pb_9 phases which are found stable, two structures at compositions $CsPb_4$ and Cs_2Pb_{17} are identified with energies of formation

Table 1
Crystallographic data of the compounds reported in the Cs-Pb system.

Phase	Space group	Lattice parameters	Ref
CsPb	I 4_1/acd (142)	a = 12.244 (1) Å c = 20.001 (2) Å	[16]
Cs_4Pb_9	P 2_1/n (14)	a = 10.042 (5) Å b = 14.781 (8) Å c = 15.863 (8) Å β = 100.17 (4)°	[17]

Table 2
Transition temperatures reported in the Cs-Pb system. The data are revised and updated based on our selected data and methodological decisions presented in Section 4.2, considering the uncertainties in the experimental measurements when available. "opt." means optimized in this work.

x (Pb)	Temperature (K)	Transition	Reaction	Enthalpy (kJ/mol.at)	Ref.
0.01	299	Eutectic	Cs(s) + α-CsPb = L	-	[15]
0.01	300	Eutectic	Cs(s) + α-CsPb = L	-	[14]
0.01	**302**	**Eutectic**	**Cs(s) + α-CsPb = L**	**-**	**This work (opt.)**
0.50	869 ± 1	Polymorphic	α-CsPb = β-CsPb	6.21	[18]
0.50	871 ± 3	Polymorphic	α-CsPb = β-CsPb	6.098 ± 0.01	[19]
0.50	**868.5**	**Polymorphic**	**α-CsPb = β-CsPb**	**6.2**	**This work (opt.)**
0.50	926	Congruent melting	β-CsPb = Liquid	3.4	[15]
0.50	893 ± 3	Congruent melting	β-CsPb = Liquid	-	[14]
0.50	920 ± 1	Congruent melting	β-CsPb = Liquid	3.99	[18]
0.50	918.3 ± 1.5	Congruent melting	β-CsPb = Liquid	3.610 ± 0.054	[19]
0.50	**923**	**Congruent melting**	**β-CsPb = Liquid**	**5.9**	**This work (opt.)**
0.55	865	Peritectic	Cs_4Pb_5 = β-CsPb + ^{L}		[15]
0.67	833	Peritectic	$CsPb_2$ = Cs_4Pb_5 + L	-	[15]
0.67	823	Peritectic	$CsPb_2$ = Cs_4Pb_5 + L	-	[14]
0.64	**818**	**Eutectic**	**L = Cs_4Pb_9 + α-CsPb**	**-**	**This work (opt.)**
0.69	**844**	**Congruent melting**	**Cs_4Pb_9 = Liquid**	**-**	**This work (opt.)**
0.75	618	Peritectic	$CsPb_3$ = $CsPb_2$ + L	-	[14]
0.75	791	Peritectic	CsPb3 = $CsPb_2$ + L	-	[15]
0.80	**616**	**Peritectic**	**$CsPb_4$ = Cs_4Pb_9 + L**	**-**	**This work (opt.)**
0.95	584	Eutectic	L = $CsPb_3$ + Pb	-	[15]
0.94	583	Eutectic	L = $CsPb_3$ + Pb	-	[14]
0.95	**579**	**Eutectic**	**L = $CsPb_4$ + Pb**	**-**	**This work (opt.)**

at 0 K that puts them close to the stability line, given the usual uncertainty of DFT computations. All of the above compositions are studied in this work by DFT calculations (see section 3). However, experimental work is needed to verify the existence of these compounds and to clarify the phase equilibria in the CsPb-Pb region.

- Liquidus data were measured by Zusman [15] and Meijer et al. [14]. The shapes of both phase diagrams are similar, but large discrepancies exist (see all experimental phase diagram data on Fig. 2). Indirect information on the liquidus shape was obtained by more recent studies into the physics of the liquid phase. Khairulin et al. [1] measured the volumetric properties of the liquid phase and reported a liquidus temperature, while Agazhanov et al. [2] measured the thermal conductivity of the liquid phase and report a table with liquidus temperatures as well. All reported transition temperatures are collected in Table 2. The data will be discussed in Section 4.2.

2.2. Chemical speciation in the liquid phase

The liquid formed after congruent melting of the CsPb compound displays short-range ordering that can be described as complexes Cs_4Pb_4, constituted of four lead ions forming a tetrahedral using covalent bonds (the so-called "Zintl polyanion" $[Pb_4]^{4-}$) surrounded by four Cs^+ cations [1,2,22,23]. The ordering in the liquid gives rise to an anomalous electrical resistivity, volume, mutual diffusion coefficient and heat capacity in the liquid state at the CsPb composition [18,19] leading to a large excess contribution. Heat capacity data will be taken into account in the thermodynamic modelling and discussed in Section 6.3.3.

2.3. Chemical speciation in the gas phase

A single study into the gas phase speciation in the Cs-Pb system was reported by Martin [24]. This study investigated Cs_nPb_m clusters and reported many heavy polyatomic clusters using mass spectrometry at a rather high ionisation potential (80 eV). Close inspection of the relative counts reveals that the most abundant ionized species are Cs^+, Cs_2^+, Pb^+ and Pb_2^+, and that these ions are detected in quantities several orders of magnitude larger than the other clusters. The corresponding neutral gaseous species are not reported. No conclusions can be draw about the neutral clusters presence or stability in gas phase.

2.4. Thermodynamic properties

Using the peak area of the measured differential calorimetry curves, Zusman [15] reported the enthalpy of fusion of CsPb (Table 2) along with the sketch of the phase diagram. No error bar was reported by the author.

Saboungi et al. [18] measured the enthalpy increment of CsPb using high-temperature drop calorimetry, revealing an α →β transition (869 K) about 50 K below the melting temperature (920 K). Recently, another enthalpy increment data set was reported by Khairulin and Stankus [19], who measured the enthalpy increment of Cs-Pb alloys containing 40, 50, 60 and 66.67 at % Pb by a high-temperature drop calorimetry method between 430 and 1075 K. The authors observed melting transitions in all Cs-Pb alloys studied at 876.7, 918.3, 802 and 839 K, respectively, and detected a solid-phase transition only in the CsPb composition at 871 K along with a possible peritectic reaction in $CsPb_2$ at 834 K. The authors provide error bars on their data (1.5 % on the enthalpy of fusion and 0.05 % on the increment enthalpy data). For CsPb, the experimental data measured by the three authors for the two phase transitions (α →β and fusion) agree very well.

Heat capacity data in CsPb have been deduced by Khairulin and Stankus [19] and Saboungi et al. [18] from their enthalpy increment measurements above 430 K.

To estimate the value of the standard entropy at 298.15 K ($S^\circ_{298.15\ K}$) of CsPb, we first plotted the heat capacity (C_p) as a function of temperature (T). At high temperatures above the threshold (T > 430 K), we applied the C_p derived on the basis of the fit model presented by Khairulin and Stankus [19]. For temperatures below this limit (T < 430 K), we performed an extrapolation to low temperatures, ensuring continuity of the C_p data for the entire temperature range. The extrapolation to low temperatures was carried out to preserve the expected temperature dependence of Cp for solids. With the Cp data for the entire temperature range, we integrated the function C_p/T with respect to temperature to calculate the entropy. This approach allowed us to estimate the entropy at 298.15 K, which was to be 110 J $mol^{-1}{\cdot}K^{-1}$.

The activity of cesium (up to 10 mol%) in molten lead was measured by Yamshchikov et al. [25] using EMF method and showed a clear temperature dependance of cesium activity in liquid lead.

2.5. Concluding remarks

According to our analysis of the experimental data, the data available for the Cs-Pb system are still limited and there are significant uncertainties in the phase diagram and the stability of Cs_xPb_y compounds. The compounds with known structures are CsPb and Cs_4Pb_9. The existence of other compounds is expected on the Pb-rich side, but their stoichiometries and structures remain unknown. Measurements of enthalpy increment, heat capacity (C_p) at high temperature, melting and transition temperatures of the CsPb compound form the relevant experimental data currently available, that are well established. Moreover, enthalpy increments were also measured in the liquid for various compositions such as $Cs_{0.33}Pb_{0.67}$, $Cs_{0.40}Pb_{0.60}$ and $Cs_{0.60}Pb_{0.40}$ as well as Cs activities in the Pb rich side. Therefore, thermodynamic properties of the liquid phase are well established. The most important deficiency is the lack of experimental data on enthalpies of formation for solid compounds, which are essential to provide a good thermodynamic description of the Cs-Pb system. In this work, DFT calculations of the energies of formation are carried out in order to fill this gap.

3. DFT calculations

3.1. Methodology

Ab initio techniques based on density-functional theory (DFT) are used to compute energies of formation and assess the thermodynamic stability of Cs_xPb_y solid compounds. One of the main challenges in DFT-based energy of formation at 0 K calculations is the selection of appropriate crystallographic structures as input data. It is common practice to use structures that have been determined experimentally, which can introduce uncertainties, e.g. for phases that undergo incompletely known phase transformations at low temperatures. By contrast, an ideal first-principles approach would rely only on chemical composition and electron count. Since the true crystallographic structure is the one that minimizes the total energy, the DFT calculation must be repeated using several candidate input structures and the reliability of the output energy increases with the number of such calculations. A second source of uncertainty is the fact that the exact exchange-correlation functional F_{xc} is unknown and the precision of available approximate functionals is also unknown. While there is no absolute guideline as to the choice of F_{xc}, in this work we rely on the recent meta-GGA flavor called R2SCAN [26].

3.2. Computational details

The DFT computations were performed using the CASTEP [27] code implementing the plane-wave pseudopotential method. The BIOVIA Materials Studio software [28] was employed to build the structures and to analyze the results. Energies of formation at 0 K were computed for all structures involved including the most stable structures of elemental Cs and Pb. To minimize the cost of the calculations, the search for the most stable structures was performed in two steps. In the first step, the PBEsol GGA exchange-correlation functional [29] was used and all 239 arbitrarily chosen candidate input structures were computed. The full list of compositions that was investigated during step 1 is displayed in Table 3 together with the number of computed structures for each composition. Their energy of formation at 0 K was plotted vs. the compound composition and the convex hull was determined. The 11 most stable among these structures were studied again using the PW91 [30] functional in order to estimate the influence of the GGA functional. In the second step, all the structures having a formation energy at 0 K within 5 kJ/mol.at of the PBEsol convex hull were selected and recomputed using more precise but also more time and memory demanding meta-GGA F_{xc}, namely RSCAN [30] and R2SCAN [26]. The corrections on mass density and energy due to spin-orbit coupling (SOC) were computed using the PBEsol functional and the resulting corrections were added to the R2SCAN results. The DFT output data used as input for elaboration of the CALPHAD model was the energy of formation of the compounds belonging to the convex hull calculated using R2SCAN and corrected for SOC.

Table 3
Chemical formula and number of structures of the Cs_xPb_y investigated compounds.

Chemical formula	Pb at. fraction	Number of structures	Chemical formula	Pb at. fraction	Number of structures
Cs1Pb0	0	2	Cs22Pb39	0.6393	1
Cs15Pb4	0.2105	1	Cs5Pb9	0.6429	1
Cs7Pb2	0.2222	1	Cs7Pb13	0.65	2
Cs13Pb5	0.2778	2	Cs1Pb2	0.6667	17
Cs5Pb2	0.2857	2	Cs4Pb9	0.6923	4
Cs9Pb4	0.3077	2	Cs2Pb5	0.7143	11
Cs8Pb5	0.3846	1	Cs1Pb3	0.75	47
Cs5Pb4	0.4444	1	Cs3Pb11	0.7857	1
Cs1Pb1	0.5	8	Cs1Pb4	0.8	7
Cs19Pb20	0.5128	2	Cs6Pb25	0.8064	1
Cs15Pb16	0.5161	1	Cs3Pb13	0.8125	1
Cs22Pb25	0.5319	1	Cs2Pb9	0.8182	1
Cs7Pb8	0.5333	5	Cs4Pb19	0.8261	1
Cs17Pb20	0.5405	1	Cs5Pb24	0.8276	1
Cs13Pb16	0.5517	1	Cs1Pb5	0.8333	1
Cs4Pb5	0.5556	34	Cs2Pb11	0.846	4
Cs16Pb21	0.5676	6	Cs3Pb17	0.85	1
Cs19Pb25	0.5682	1	Cs4Pb23	0.8518	1
Cs3Pb4	0.5714	21	Cs1Pb6	0.8571	1
Cs8Pb11	0.5789	1	Cs5Pb32	0.8649	1
Cs13Pb18	0.5806	1	Cs1Pb7	0.875	9
Cs12Pb17	0.5862	13	Cs3Pb23	0.8846	1
Cs2Pb3	0.6	8	Cs2Pb17	0.8947	2
Cs8Pb13	0.6190	1	Cs1Pb16	0.9412	1
Cs3Pb5	0.625	1	Cs1Pb17	0.9444	1
Cs7Pb12	0.6316	1	Cs0Pb1	1	1

Each DFT computation consisted of a geometry optimization of the input structure using the BFGS algorithm [31]. The "2017R2" and "SOC19" ultrasoft pseudopotentials libraries were used [28,32]. The calculation parameters are described in Annex 1. Except for CsPb, $Cs_{12}Pb_{17}$ and Cs_4Pb_9, all the investigated compounds had a metallic band structure. This led to the choice of a rather dense Brillouin zone sampling for the precise set of calculations.

The numerical parameters reported in columns 3 ("Step 2″) and 4 ("Step 3″) of Annex 1 were set so as to ensure a numerical precision of 0.1 kJ/mol.at on the energy of formation at 0 K. As can be seen from Table 3, a special effort was devoted to identify stable structures having compositions close to Cs_4Pb_5, $CsPb_2$ and $CsPb_3$ which were suggested by previous experimental work as reported in Section 2. The input crystallographic structures included experimentally known compositions such as Cs, CsPb (SG142), Cs_4Pb_9 (SG14), and Pb, $CsPb_4$ (SG139) and Cs_2Pb_{17} (SG194), the latter being taken from the OQMD database [21]. Many structures of known A_xM_y compounds have been tested in which A is an alkaline element and M is a group IV_A element. Structures of known compounds having the desired stoichiometry with other chemical elements, were finally completed by some arbitrarily constructed structures. The most stable DFT optimized structures are reported in the Supplementary material.

The energies of formation ΔH_f ($Cs_{1-x}Pb_x$) at 0 K are given by the following expression:

$$\Delta H_f(Cs_{1-x}Pb_x) = \mathrm{E}(Cs_{1-x}Pb_x) - ((1-\mathrm{x})\,\mathrm{E}(Cs) + \mathrm{x}\;\;\mathrm{E}(Pb)) \quad (1)$$

where $E(Cs_{1-x}Pb_x)$, E(Cs) and E(Pb) are the energies per atom of the compound $Cs_{1-x}Pb_x$ and the pure species Cs and Pb at 0 K. These $\Delta H_f(Cs_{1-x}Pb_x)$ data will be used in the thermodynamic modelling of the Cs-Pb system assuming that the energy of formation of the compounds does not change significantly from 0 K to 298.15 K. Since we did not compute any phonon spectrum, we neglect the zero-point contributions to the energy and pressure. In other words, we approximate the energy by the

static energy and the zero-pressure volume by the static volume, both quantities being the output of the DFT codes.

3.3. Computational results

In agreement with experimental data from the literature [16,17,21], the compounds CsPb and Cs_4Pb_9 were found stable. After testing 239 structures, the screening with PBEsol suggests that only $Cs_{12}Pb_{17}$ and $CsPb_4$ might also be stable (Fig. 1a). More refined calculations with R2SCAN + SOC confirmed $CsPb_4$ as stable at T = 0 K, while $Cs_{12}Pb_{17}$ remains 0.1 kJ/mol.at above the convex hull and thus potentially stable too (Fig. 1b). The compound with Cs_2Pb_{17} composition taken from Ref. [21] is 2.3 kJ/mol.at above the convex hull and is thus likely unstable. Uncertainties remain due to potentially missed stable structures and to the influence of vibrational contributions which were not computed. While the existence of phases with composition $CsPb_3$ and Cs_4Pb_5 was suggested in Ref. [8] from DSC data, we did not identify structures having these exact compositions which would be stable at 0 K. Since Meijer [14] explicitly states that no attempt was made to determine the exact composition of these otherwise unknown phases, and their reported formulas should therefore be considered approximate, for the CALPHAD model, we kept only the compounds with the most stable structures predicted by DFT, i.e. Cs_4Pb_9 and $CsPb_4$ in addition to CsPb.

Table 4 presents the final DFT results, including formation energies at T = 0 K which will be used for further thermodynamic assessments. For comparison purposes, we have included the energy of formation values for the considered compounds reported in the OQMD database [21].

As shown in Fig. 1a and Table 4, the OQMD values are consistent with our PBEsol results, whereas the R2SCAN + SOC calculations

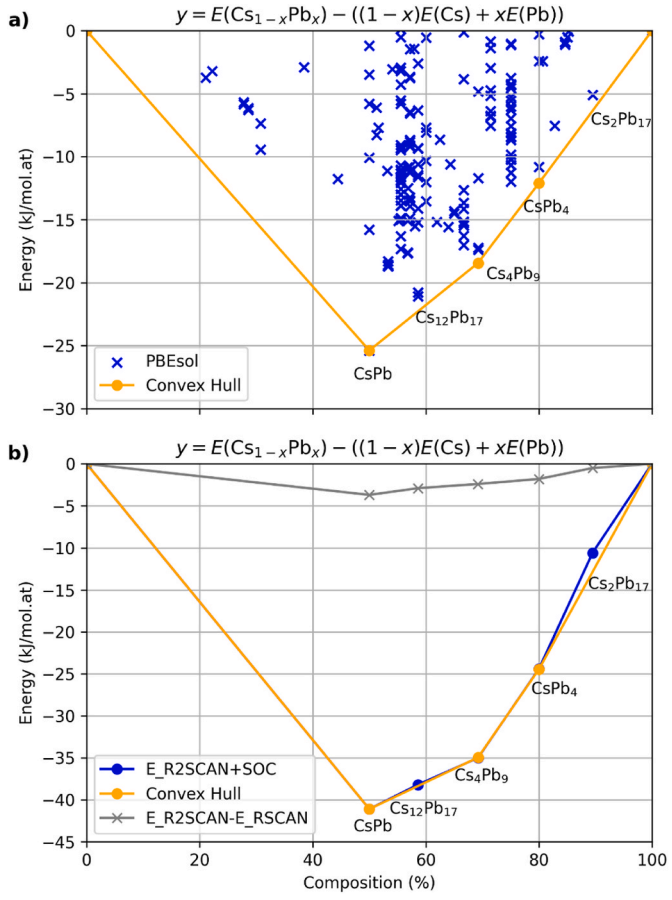


Fig. 1. DFT energy of formation at 0 K of the proposed structures with different exchange-correlation functionals (a) PBEsol (b) R2SCAN + SOC.

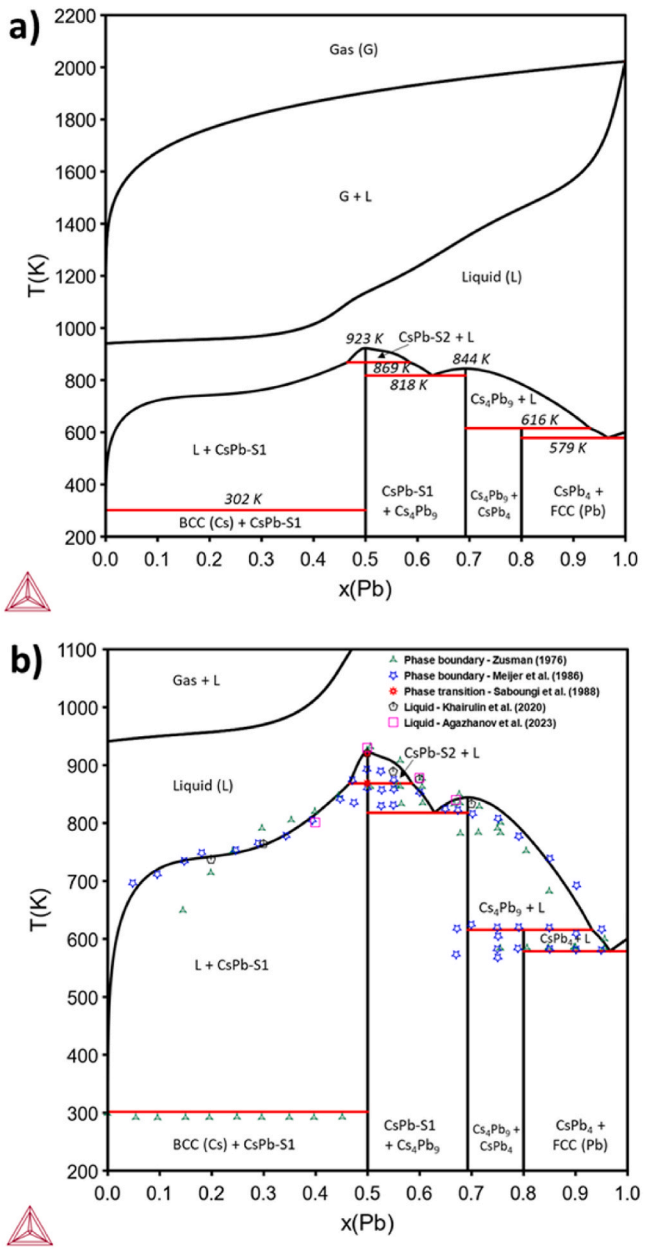


Fig. 2. Cs-Pb phase diagram calculated in this study (black line) compared with experimental data with (a) and without (b) the gas phase.

Table 4
DFT energies of formation at T = 0 K for the identified stable compounds, computed with R2SCAN and corrected for SOC compared to those from OQMD database.

Compound	x (Pb)	Energy of formation (kJ/mol.at)	Energy of formation from OQMD (kJ/mol.at)
CsPb	0.50	−41.1	−24.41
Cs_4Pb_9	0.692	−35.0	−19.77
$CsPb_4$	0.80	−24.4	−11.09

(Fig. 1b and Table 4) yield substantially more negative formation energies, almost twice as high, reflecting the strong influence of the exchange-correlation functional.

The optimized crystallographic structures are given in the supplemental material. CsPb is the compound with the largest formation enthalpy. This is consistent with its high melting point compared to the

other Pb rich compounds.

In conclusion, our DFT computations suggest that at low temperatures the stable phases are CsPb, Cs_4Pb_9 and $CsPb_4$. However, we cannot exclude the possibility that other compounds with different stoichiometries may be stable at higher temperatures. New experiments are needed to check the existence of all the compounds. The DFT computed formation enthalpies for CsPb, Cs_4Pb_9 and $CsPb_4$ are taken into account in the CALPHAD model described in the subsequent section.

4. Thermodynamic modelling

The CALPHAD method is widely used for thermodynamic assessments and phase diagram calculations, aiding the development of databases describing Gibbs energies of various solid, liquid, and gas phases as a function of temperature, composition, and pressure. In this work, the calculations were performed by means of Thermo-Calc software, version 2024a [33]. The CALPHAD method consists of optimizing Gibbs energy functions of the solid, liquid and gas phases to reproduce the experimentally observed phase equilibria and measured or calculated thermodynamic properties (enthalpy of formation, standard entropy, enthalpy increments, heat capacity, vapor pressures and activities). All Gibbs energies are referenced to the Stable Element Reference (SER) state, which corresponds to the state of the element at T = 298.15 K and p = 10^5 Pa.

4.1. Models

The Gibbs energy function G_i^{Φ} for 1 mol of the pure element i in the Φ structure, relative to the Standard Element Reference (SER) state is modelled using:

$$G_i^{\Phi} - H_i^{SER} = a + bT + cTlnT + \sum d_n T^n \quad (2)$$

Here, n is an integer for additional terms and usually takes values 2, 3, −1. The term H_i^{SER} is the molar enthalpy of the element i in its stable state at 298.15 K and 1 bar. The coefficients a, b, c, and d_n are model parameters.

The Gibbs energies for pure cesium in body-centered cubic (BCC-A2) and liquid phase are taken from the SGTE pure elements database [34]. In the same way, the data for lead in face-centered cubic (FCC-A1) structure and liquid phase is taken from the same database.

For the gas phase, the Gibbs energy functions for the gaseous species (Cs,Cs_2,Pb,Pb_2) have been taken from the SSUB5 substance database [35]. The clusters Cs_xPb_y(g) cannot be taken into account as no thermodynamic data exist on these gaseous species.

4.2. Stoichiometric compounds

The CsPb compound is described by the sublattice model (Cs^{+1})(Pb^{-1}) to link its structure with the one of the liquid (see section 4.1.2). The two crystalline forms are described: CsPb-S1 and CsPb-S2. For CsPb-S1, the low temperature form, the corresponding Gibbs energy function is expressed in the following general form:

$$G^{CsPb-S1} - \sum_i n_i^{\Phi} H_i^{SER} = a + bT + cTlnT + \sum d_n T^n \quad (3)$$

Here, n_i^{Φ} represents the stoichiometric coefficient of element i in the compound. The coefficients have been optimized to fit experimental data on enthalpy increment, and energy of formation from DFT. Moreover, heat capacity data deduced from enthalpy measurements were used as well. The experimental transition enthalpy and temperature have been used to describe the CsPb-S2 form.

Cs_4Pb_9 and $CsPb_4$ are represented in stoichiometric notation as $(Cs)_P(Pb)_Q$.

For these compounds, for which no heat capacity or enthalpy increment data are available, the Kopp-Neumann relation leads to the appearance of discontinuities due to the phase transitions in the pure elements, especially at the Cs melting point. Therefore, this relation could not be used. As a starting point, for both compounds, we took the same Cp function as for CsPb-S1 multiplied by a factor equal to the ratio of the number of atoms in Cs_xPb_y to the number of atoms in CsPb. The heat capacity functions for both compounds are as follows:

$$G^{Cs4Pb9} - \sum_i n_i^{\Phi} H_i^{SER} = a1 + b1\ T + c1\ TlnT + 6.5\left(cTlnT + \sum d_n T^n\right) \quad (4)$$

$$G^{CsPb4} - \sum_i n_i^{\Phi} H_i^{SER} = a2 + b2\ T + 2.5\left(cTlnT + \sum d_n T^n\right) \quad (5)$$

For Cs_4Pb_9, the Cp coefficient c1 has been adjusted to fit the enthalpy increment data in $Cs_{0.4}Pb_{0.6}$ and $Cs_{0.33}Pb_{0.67}$ measured in the solid state by Khairulin and Stankus [19]. No extra coefficient could be fitted for $CsPb_4$ as no enthalpy data are available in this composition range.

The values of a, a1, a2 and b, b1, b2 were optimized using DFT calculations and phase diagram data.

4.3. Liquid

The two-sublattice partially ionic liquid model developed by Hillert et al. [23] was applied to describe the Cs-Pb liquid phase using the sublattice model $(Cs^{+1})_P(Pb^{-1},Va^{-Q},Pb)_Q$. "Va" denote vacancies included on the anionic sublattice to describe pure liquid Cs as (Cs^{+1})(Va^{-1}). These vacancies have a variable charge -Q to maintain overall charge neutrality within the ionic model.

The species Pb^{-1} has been introduced in the second sublattice to account for short-range ordering in the liquid with the formation of Cs_4Pb_4 clusters according to Refs. [18,19,22,23]. In our model, the clusters are described by the end-member (Cs^{+1}) (Pb^{-1}). Pure liquid Cs is described by the end-member (Cs^{+1}) (Va^{-1}) and pure liquid lead is represented by the neutral species "Pb" in the second sublattice.

P and Q, the numbers of sites on the cation and anion sublattices respectively, vary as a function of the composition in order to maintain electroneutrality and are equal to the sum of the products of species charge and site fraction of the second and first sublattices, respectively:

$$P = y_{Pb^{-1}} + y_{Va^{-1}} \quad (6)$$

$$Q = y_{Cs^{+1}} = 1 \quad (7)$$

where y_i is the site fraction of each species i in their own sub-lattices in the liquid phase. In Eq. (6) the neutral atoms Pb are not included in the relation since they carry no charge and therefore do not contribute to the charge balance. The Gibbs energy of the liquid phase is defined as:

$$G^{liq} = G^{ref} + G^{ideal} + G^{xs} \quad (8)$$

The first term G^{ref} denotes the reference Gibbs energy term corresponding to a mechanical mixture of the end-members. The term G^{ideal} accounts for ideal mixing (i.e. configurational entropy contribution), while G^{xs} represents the excess term. The Gibbs energy expression for the liquid is given as follows:

$$G^{ref} = y_{Pb^{-1}} G^{Liq}_{Cs^{+1}:Pb^{-1}} + y_{Pb} G^{Liq}_{Pb} + y_{Va^{-1}} G^{Liq}_{Cs^{+1}:Va^{-1}} \quad (9)$$

$$G^{ideal} = \mathrm{RT}\left(y_{Pb^{-1}}\ ln\, y_{Pb^{-1}} + y_{Pb}\ ln\, y_{Pb} + y_{Va^{-1}}\ ln\, y_{Va^{-1}}\right) \quad (10)$$

$$G^{xs} = y_{Va^{-1}}\ y_{Pb^{-1}}\ L^{Liq}_{Cs^{+1}:Va^{-1},Pb^{-1}} + y_{Pb}\ y_{Pb^{-}}\ L^{Liq}_{Cs^{+1}:Pb,Pb^{-1}} \quad (11)$$

The interaction parameter expressed as $L^{Liq}_{Cs^{+1}:i,j}$ represents the interaction between i and j in the second sublattice, which is commonly expanded with a Redlich–Kister (RK) polynomial function [36] as:

$$L_{i,j}^{Liq} = \sum_k {}^{k}L_{i,j}^{liq}\left(y_i - y_j\right)^k \quad (12)$$

with $k = 0$, 1 and 2.

The parameters ${}^{k}L_{i,j}^{liq}$ can be temperature dependent:

$${}^{k}L_{i,j}^{liq} = a_k + b_k.T \quad (13)$$

where a_k and b_k were optimized in this work. It should be noted that composition dependent interaction parameters (${}^{k}L_{i,j}^{liq}$ with $k = 0$, 1 and 2) were required to adequately model the experimental data of the liquid phase over the whole relevant composition and temperature range.

4.4. Selected data

Table 5 provides an overview of the thermodynamic and phase diagram data selected in this study, indicating which data were used or excluded for the modelling, classified in three main categories.

First, the phase transition temperature data reported by Meijer et al. [14] together with the experimental phase transition and melting temperature data for CsPb measured by calorimetry [18,19] have been selected as these data are considered to be carefully measured. However, the phase diagram measurements [14] have been reinterpreted assuming the existence of CsPb, Cs_4Pb_9 and $CsPb_4$. Second, for the thermodynamic data, we incorporated enthalpy increments for $Cs_{0.50}Pb_{0.50}$, $Cs_{0.33}Pb_{0.67}$, $Cs_{0.40}Pb_{0.60}$ and $Cs_{0.60}Pb_{0.40}$ as reported in Refs. [18,19] and activity measurements in Ref. [25], to describe the variation of liquid thermodynamic properties across the compositional range. To complement the experimental dataset, we used first-principles DFT calculations to obtain the energies of formation and structural data for compositions not fully covered by experiments. This includes values for compounds CsPb, Cs_4Pb_9 and $CsPb_4$. These ab initio results enhance the consistency and completeness of the thermodynamic assessment by filling experimental gaps and supporting the evaluation of phase stability of solid compounds. This large database supports both the assessment of phase stability and the development of reliable thermodynamic models.

5. Optimization process

The Gibbs energy parameters were adjusted using the PARROT module of the Thermo-Calc software. This was done using a step-by-step approach to ensure consistency with available thermodynamic and phase equilibrium information. The PARROT module allows to simultaneously consider different sets of experimental data, weighted according to their uncertainty. Our assessment is applicable to temperatures from 298.15 K. The formation energies of CsPb, Cs_4Pb_9 and $CsPb_4$ estimated by DFT calculations at 0 K are used as the initial parameters in the present optimization.

The optimization was performed in the following steps: First, the Gibbs energy parameters of CsPb were optimized using experimental enthalpy increment data, heat capacity data, DFT-based energy of formation value as well as the estimated standard entropy. Once a reliable Gibbs energy for solid CsPb had been established, its parameters were fixed, and the optimization proceeded to the liquid phase. In this phase, interaction parameters were adjusted and the additional compounds (Cs_4Pb_9 and $CsPb_4$) were incorporated into the fitting process.

Table 5
Summary of the thermodynamic data used in this study indicating selection status and references.

Data	Selected/Not selected	Ref
Phase diagram data	Selected	[14]
Phase diagram data	Not selected	[15]
Enthalpy increment for $Cs_{0.5}Pb_{0.5}$	Selected	[18,19]
Enthalpy increment for $Cs_{0.33}Pb_{0.67}$, $Cs_{0.40}Pb_{0.60}$ and $Cs_{0.60}Pb_{0.40}$	Selected	[19]
Transition enthalpy of CsPb	Selected	[18]
Melting enthalpy of CsPb	Selected	[18,19]
Transition temperature of CsPb	Selected	[18]
Melting temperature of CsPb	Selected	[18,19]
Heat Capacity of CsPb	Selected	[18,19]
$S^{\circ}_{298.15\ K}$ of CsPb	Selected	This work (graphical fit)
Cs_4Pb_5 compound	Not selected	[14,15], This work (DFT)
Cs_4Pb_9 compound	Selected	[14,15], This work (DFT)
$CsPb_3$ compound	Not selected	[14,15], This work (DFT)
$Cs_{12}Pb_{17}$	Not selected	This work (DFT)
$CsPb_4$ compound	Selected	This work (DFT)
Cs_2Pb_{17}	Not selected	This work (DFT)
Activities	Selected	[25]

6. Results and discussion

6.1. The optimized thermodynamic parameters

The final optimized thermodynamic parameters of the Cs-Pb system are listed in Table 6.

6.2. Phase diagram

Fig. 2 shows the calculated phase diagram compared with experimental data from the literature [1,2,14,15,18]. The calculated temperature data for the invariant transitions are reported in Table 2. An overall agreement is found with the experimental data.

The α→β transition and melting point for CsPb are very well reproduced. The sharp shape of the phase diagram at the $Cs_{0.5}Pb_{0.5}$ composition is well described by the ionic model, which accounts for short-range ordering in the liquid. The liquidus line is very well captured on the Cs-CsPb side, the liquidus is also reasonably well reproduced on the CsPb-Pb side, although there are greater uncertainties due to the limited reliability of the experimental data in this region. The model is not able to reproduce the peritectic decomposition of Cs_4Pb_9, proposed in Refs. [14,15]. Instead, it shows a congruent melting behaviour along with a eutectic reaction (Liq = CsPb + Cs_4Pb_9), which takes place at a temperature about 5 K lower than that the invariant of Meijer et al. [14]. Increasing the temperature of this plateau led to an overestimation of the enthalpy increase at the $Cs_{0.4}Pb_{0.6}$ composition. We have decided to give more weight to the liquid phase enthalpy measurements, which were performed with satisfactory accuracy. New experimental work would be beneficial to better describe this part of the phase diagram. At lower temperatures, the liquidus is adequately represented in the (Liq + Cs_4Pb_9) region. However, the phase transitions between $CsPb_4$ and Cs_4Pb_9 are uncertain. The two transitions preceding $CsPb_4$, observed by both Meijer [14] and Zusman [15], suggest the presence of intermediate phases. Their precise nature remains unclear, highlighting the need for targeted solid-state synthesis experiments to confirm and characterize these phases. To conclude, the phase diagram will have to be experimentally studied in the CsPb-Pb section to complete the existing data and confirm the nature of the stable compounds, the invariant reactions involving Cs_4Pb_9 and $CsPb_4$, particularly, the formation of Cs_4Pb_9 in the eutectic reaction, and the peritectic decomposition of $CsPb_4$.

6.3. Thermodynamic data

6.3.1. DFT results

Table 7 groups the values of the enthalpy of formation of CsPb, Cs_4Pb_9 and $CsPb_4$ calculated by our CALPHAD model for T = 298.15 K and those found by DFT calculations at T = 0 K. A good agreement is obtained. The table also reports the optimized thermodynamic parameters using CALPHAD.

Table 6
Optimized thermodynamic parameters for the Cs-Pb binary system. Temperature range from 298.15 K to 10,000 K.

Phase: Model	Thermodynamic parameters (J.mol^{-1})	Reference
Gas (Cs,Cs_2,Pb,Pb_2)	${}^{\circ}G^{Gas}_{Cs} - H^{SER}_{Cs} = \mathrm{GCSGAS} + \mathrm{RTln}(10^{-5}\ \mathrm{P})$	SSUB5 [35]
	${}^{\circ}G^{Gas}_{Cs_2} - 2\,H^{SER}_{Cs} = \mathrm{GCS2GAS} + \mathrm{RTln}(10^{-5}\ \mathrm{P})$	SSUB5 [35]
	${}^{\circ}G^{Gas}_{Pb} - H^{SER}_{Pb} = \mathrm{GPBGAS} + \mathrm{RTln}(10^{-5}\ \mathrm{P})$	SSUB5 [35]
	${}^{\circ}G^{Gas}_{Pb_2} - 2\,H^{SER}_{Pb} = \mathrm{GPB2GAS} + \mathrm{RTln}(10^{-5}\ \mathrm{P})$	SSUB5 [35]
Liquid: $(Cs^{+1})_1(Pb^{-1}, Va, Pb)_1$	${}^{\circ}G^{Liq}_{Pb} - H^{SER}_{Pb} = +\mathrm{GLIQPB}$	PURE5 [37]
	${}^{\circ}G^{Liq}_{Cs^{+1}:Va^{-1}} - H^{SER}_{Cs} = +\mathrm{GLIQCS}$	PURE5 [37]
	${}^{\circ}G^{Liq}_{Cs^{+1}:Pb^{-1}} - H^{SER}_{Cs} - H^{SER}_{Pb} = GCSPBS2$	This work
	$+ 7980 - 8.1049\ T$	This work
	${}^{0}L\left(Cs^{+1} : Pb^{-1}, Va\right) = +9055$	This work
	${}^{1}L\left(Cs^{+1} : Pb^{-1}, Va\right) = -3217$	This work
	${}^{2}L\left(Cs^{+1} : Pb^{-1}, Va\right) = +2102$	This work
	${}^{0}L\left(Cs^{+1} : Pb^{-1}, Pb\right) = -16425 + 12.98\ T$	This work
	${}^{1}L\left(Cs^{+1} : Pb^{-1}, Pb\right) = +16783 - 10.296\ T$	This work
	${}^{2}L\left(Cs^{+1} : Pb^{-1}, Pb\right) = +8662$	This work
CsPb-S1: $(Cs^{+1})\ (Pb^{-1})$	${}^{\circ}G_{CsPb-S1} - H^{SER}_{Cs} - H^{SER}_{Pb} = GCSPBS1$	This work
CsPb-S2: $(Cs^{+1})\ (Pb^{-1})$	${}^{\circ}G_{CsPb-S2} - H^{SER}_{Cs} - H^{SER}_{Pb} = GCSPBS2$	This work
Cs_4Pb_9: $(Cs)_4(Pb)_9$	${}^{\circ}G_{Cs4Pb9} - 4\,H^{SER}_{Cs} - 9\,H^{SER}_{Pb} = -551500 + 1867\ T - 40\ Tln(T) + 6.5\ FCSPB$	This work
$CsPb_4$: $(Cs)_1(Pb)_4$	${}^{\circ}G_{CsPb4} - H^{SER}_{Cs} - 4\,H^{SER}_{Pb} = -162000 + 613\ T + 2.5\ FCSPB$	This work
BCC: $(Cs,Pb)_1(Va)_3$	${}^{\circ}G^{BCC}_{Cs:Va} - H^{SER}_{Cs} = +\ GHSERCS$	PURE5 [37]
	${}^{\circ}G^{BCC}_{Pb} \circ G^{BCC}_{Pb:VaA} - H^{SER}_{Pb} = +\ GBCCPB$	PURE5 [37]
	${}^{0}L(Cs, Pb : Va) = +5000$	This work
FCC: (Cs,Pb) (Va)	${}^{\circ}G^{FCC}_{Pb:Va} - H^{SER}_{Pb:Va} = +\ GHSERPB$	PURE5 [37]
	${}^{\circ}G^{FCC}_{Cs:Va} - H^{SER}_{Cs:Va} = +\ GFCCCS$	PURE5 [37]
	${}^{0}L(Cs, Pb : Va) = +50000$	This work
Functions	$FCSPB = -52.9456268\ T\ln(T) + 4.82591517.10^{-3}\ T^2 + 42312.8378\ T^{-1} - 4.39945721.10^{-6}\ T^3$	This work
	$GCSPBS1 = -98200 + 243\ T + FCSPB$	This work
	$GCSPBS2 = GCSPBS1 + 12420 - 14.3\ T$	This work
	GLIQPB	PURE5 [37]
	$298.15 < T < 600.61 : + GHSERPB + 4672.124 - 7.750683\ T - 6.019.10^{-19}\ T^7$	
	$600.61 < T < 1200 : -5677.958 + 146.176046\ T - 32.4913959\ T\ ln(T)$	
	$+ .00154613\ T^2$	
	$1200 < T < 6000 : + 9010.753 + 45.071937\ T - 18.9640637\ T\ ln(T)$	
	$- .002882943\ T^2 + 9.8144.10^{-8}\ T^3 - 2696755\ T^{-1}$	
	GHSERPB	PURE5 [37]
	$298.15 < T < 600.61 : -7650.085 + 101.700244\ T - 24.5242231\ T\ ln(T)$	
	$- .00365895\ T^2 - 2.4395.10^{-7}\ T^3$	
	$600.61 < T < 1200 : -10531.095 + 154.243182\ T - 32.4913959\ T\ ln(T)$	
	$+ .00154613\ T^2 + 8.05448.10^{25}\ T^{-9}$	
	$1200 < T < 6000 : + 4157.616 + 53.139072\ T - 18.9640637\ T\ ln(T)$	
	$- .002882943\ T^2 + 9.8144.10^{-8}\ T^3 - 2696755\ T^{-1} + 8.05448.10^{25}\ T^{-9}$	
	GLIQCS	PURE5 [37]
	$298.15 < T < 301.59 : + GHSERCS + 2091.141 - 6.931035\ T - 3.56867.10^{-18}\ T^7$	
	$301.59 < T < 6000 : -11454.038 + 211.728844\ T - 46.7273304\ T\ ln(T)$	
	$+ .02043269\ T^2 - 4.074846.10^{-6}\ T^3 + 181528\ T^{-1}$	
	GHSERCS	PURE5 [37]
	$298.15 < T < 301.59 : -17373.82 + 436.899787\ T - 90.5212584\ T\ ln(T)$	
	$+ .2029422\ T^2 - 1.27907669.10^{-4}\ T^3 + 245245\ T^{-1}$	
	$301.59 < T < 6000 : -13553.817 + 218.689955\ T - 46.7273304\ T\ ln(T)$	
	$+ .02043269\ T^2 - 4.074846.10^{-6}\ T^3 + 181528\ T^{-1} + 7.8016.10^{21}\ T^{-9}$	
	$GFCCCS = +\ GHSERCS + 500 + 1.3\ T$	PURE5 [37]
	$GBCCPB = +\ GHSERPB + 2400 - 1.1\ T$	PURE5 [37]
	GCSGAS	SSUB5 [35]
	$298.15 < \mathrm{T} < 1600 : + 70221.1857 - 34.9432617\ \mathrm{T} - 21.01225\ \mathrm{T\ ln(T)}$	
	$+ 2.3869595.10^{-4}\ T^2 - 4.17045667.10^{-8}\ T^3 + 4922.448\ T^{-1}$	
	$1600 < \mathrm{T} < 3400 : + 65030.9624 + 16.0373197\ \mathrm{T} - 28.23664\ \mathrm{T\ ln(T)}$	
	$+ .0041988735\ T^2 - 4.22771.10^{-7}\ T^3 + 522968.5\ T^{-1}$	

(*continued on next page*)

Table 6 (*continued*)

Phase: Model	Thermodynamic parameters (J.mol^{-1})	Reference
	$3400 < T < 5300 : +366608.608 - 1031.64395\,T + 100.1023\,T\ln(T) - .020285495\,T^2 + 4.61329.10^{-8}\,T^3 - 1.333813.10^8\,T^{-1}$ $5300 < T < 7000 : +21277.4247 - 330.32731\,T + 20.43107\,T\ln(T) - .012545005\,T^2 + 3.32779833.10^{-7}\,T^3 + 1.375229.10^8\,T^{-1}$ $7000 < T < 10000 : -1347367.73 + 2313.0949\,T - 278.8398\,T\ln(T) + .016571635\,T^2 - 1.98924.10^{-7}\,T^3 + 1.3125275.10^9\,T^{-1}$	
	GCS2GAS $298.15 < T < 700 : +100114.046 - 81.8752338\,T - 29.1921\,T\ln(T) - .01584241\,T^2 + 4.411035.10^{-6}\,T^3 - 87527.95\,T^{-1}$ $700 < T < 1700 : +76365.6162 + 232.868668\,T - 76.74226\,T\ln(T) + .026454175\,T^2 - 2.64218333.10^{-6}\,T^3 + 2135020\,T^{-1}$ $1700 < T < 3000 : +250375.533 - 857.020867\,T + 68.80663\,T\ln(T) - .028077265\,T^2 + 1.22328533.10^{-6}\,T^3 - 37126965\,T^{-1}$ $3000 < T < 4900 : -161131.901 + 641.492817\,T - 115.7658\,T\ln(T) + .008419445\,T^2 - 1.1690215.10^{-7}\,T^3 + 1.3370865.10^8\,T^{-1}$ $4900 < T < 6000 : -155428.026 + 692.773744\,T - 122.889\,T\ln(T) + .01069752\,T^2 - 2.11018.10^{-7}\,T^3 + 1.1397085.10^8\,T^{-1}$	SSUB5 [35]
	GPBGAS $298.15 < T < 1100 : +191972.908 - 34.214593\,T - 21.30643\,T\ln(T) + 6.551465.10^{-4}\,T^2 - 1.4308295.10^{-7}\,T^3 + 9337.21\,T^{-1}$ $1100 < T < 2000 : +189554.946 - .102464321\,T - 26.43463\,T\ln(T) + .004836378\,T^2 - 7.36003167.10^{-7}\,T^3 + 151170.2\,T^{-1}$ $2000 < T < 3700 : +287755.457 - 557.708056\,T + 46.90369\,T\ln(T) - .01960158\,T^2 + 7.96842.10^{-7}\,T^3 - 24599010\,T^{-1}$ $3700 < T < 5200 : -76463.6581 + 670.919164\,T - 102.9479\,T\ln(T) + .007928075\,T^2 - 1.55617667.10^{-7}\,T^3 + 1.4219575.10^8\,T^{-1}$ $5200 < T < 8200 : -177763.071 + 936.081131\,T - 134.2151\,T\ln(T) + .01228287\,T^2 - 2.70638667.10^{-7}\,T^3 + 2.0490225.10^8\,T^{-1}$ $8200 < T < 8200.01 : +1430486.92 - 1724.85376\,T + 161.2387\,T\ln(T) - .011905435\,T^2 + 1.01633317.10^{-7}\,T^3 - 1.440972.10^9\,T^{-1}$	SSUB5 [35]
	GPB2GAS $298.15 < T < 1400 : +295916.393 - 30.4287511\,T - 36.885\,T\ln(T) - .001044156\,T^2 - 1.93234833.10^{-8}\,T^3 - 834.586\,T^{-1}$ $1400 < T < 2300 : +309949.845 - 91.5566147\,T - 29.46399\,T\ln(T) - .001186672\,T^2 - 2.884025.10^{-7}\,T^3 - 3780887\,T^{-1}$ $2300 < T < 3500 : +402211.8 - 645.429872\,T + 43.76939\,T\ln(T) - .02616466\,T^2 + 1.27101733.10^{-6}\,T^3 - 24494475\,T^{-1}$ $3500 < T < 6000 : -88356.1217 + 1152.58425\,T - 178.0027\,T\ln(T) + .018362105\,T^2 - 4.039735.10^{-7}\,T^3 + 1.7883455.10^8\,T^{-1}$	SSUB5 [35]

Future experimental measurements of the formation enthalpy and heat capacity for Cs_4Pb_9 and $CsPb_4$ as well as synthesis and characterization of hypothetical $CsPb_2$ and $CsPb_3$ compounds are recommended to validate the calculated thermodynamic properties of these compounds.

6.3.2. *Enthalpy increment*

The calculated enthalpy increment H(T)-H(298.15 K) are reported in Fig. 3. A good agreement is found with measured data for $Cs_{0.5}Pb_{0.5}$ reported in Refs. [18,19]. In the work of Saboungi et al. [18], the transition temperature (T_t) is reported to be 869 ± 1 K, with a transition enthalpy ($\Delta_{trs}H$) of 6.21 kJ/mol.at. In the study of Khairulin and Stankus [19], the T_{trs} is reported as 871 ± 3 K, with a $\Delta_{trs}H$ of 6.098 ± 1.0 kJ/mol.at.

In the present study, T_{trs} is 868.5 K, with a $\Delta_{trs}H$ of 6.2 kJ/mol.at, demonstrating a good agreement with the experimental results. The melting temperature has been discussed previously, and the melting enthalpy ($\Delta_{fus}H$) was found to be 3.99 kJ/mol.at from Saboungi et al. [18] and 3.61 ± 0.054 kJ/mol.at from Khairulin and Stankus [19].

Our CALPHAD-based model gives a melting enthalpy for $Cs_{0.5}Pb_{0.5}$ of 5.9 kJ mol^{-1}, higher by ~1.91 kJ mol^{-1} and ~2.29 kJ mol^{-1} compared to the values from Saboungi et al. [18] and Khairulin and Stankus [19], respectively. Similarly, the enthalpy increment data of $Cs_{0.33}Pb_{0.67}$, $Cs_{0.40}Pb_{0.60}$ and $Cs_{0.60}Pb_{0.40}$ obtained in our model agree well with the experimental values reported in Ref. [19] especially in the solid state, as seen in Fig. 3 b), c) and d). The uncertainties given in Ref. [19] are very low, equal to 0.05 %, which reflects high reproducibility of the measurements. It was not possible to get a good agreement in the model for both the phase diagram in the region CsPb-Cs_4Pb_9 and the enthalpy increment for $Cs_{0.40}Pb_{0.60}$ and $Cs_{0.33}Pb_{0.67}$. As already mentioned, the phase equilibria in this region are still uncertain. The maximum deviations of the calculated values from the experimental data in the liquid are approximately of 3-4%, 1-2%, 4-8 % and 4-5 % for $Cs_{0.33}Pb_{0.67}$, $Cs_{0.50}Pb_{0.50}$, $Cs_{0.40}Pb_{0.60}$ and $Cs_{0.60}Pb_{0.40}$, respectively. The increment

Table 7
Calculated formation enthalpy, standard entropy and Gibbs energy of formation values of the compounds. Comparison with DFT data.

Compound	ΔH_f (DFT) (kJ/mol.at) at T = 0 K	$\Delta H^\circ_{f\ 298.15\ K}$ (CALPHAD) (kJ/mol.at)	$S^\circ_{298.15\ K}$ (CALPHAD) (J/mol.at.K)	$Cp_{298.15\ K}$ (CALPHAD) (J/mol.at.K)	$\Delta G^\circ_{f\ 298.15\ K}$ (CALPHAD) (kJ/mol.at)
CsPb	−41.1	−41.16	55.19	25.73	−57.61
Cs_4Pb_9	−34.9	−33.57	53.68	28.77	−49.57
$CsPb_4$	−24.4	−24.46	54.09	25.73	−40.59

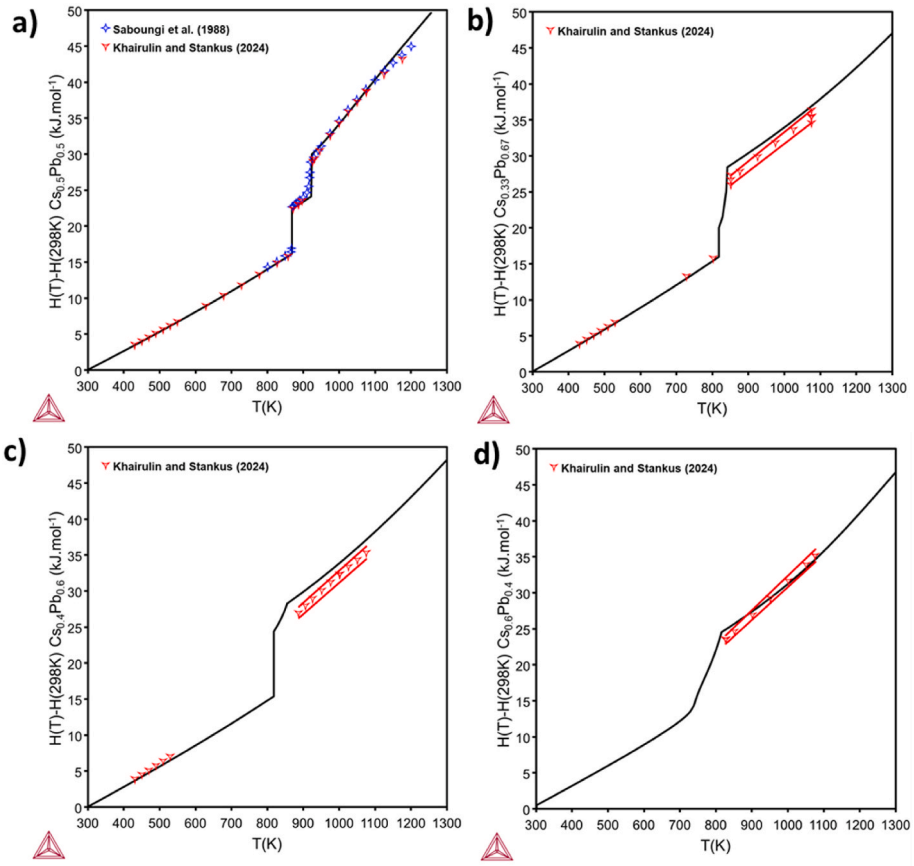


Fig. 3. Calculated enthalpy increment (black line) of a) $Cs_{0.50}Pb_{0.50}$, b) $Cs_{0.33}Pb_{0.67}$, c) $Cs_{0.40}Pb_{0.60}$ and d) $Cs_{0.60}Pb_{0.40}$ compared with experimental data. The red lines represent experimental uncertainty margins.

enthalpy of CsPb in the liquid exhibits an arc-like shape, which diminishes as the temperature increases. This observation explains the heat capacity behavior of CsPb liquid at high temperatures, which will be discussed in the next section.

6.3.3. *Heat capacity*

Fig. 4a illustrates the calculated heat capacity (C_p) of CsPb which exhibits an unusual thermal characteristic. Notably, the C_p undergoes a steep increase at the melting point followed by a subsequent decrease at high temperatures. This steep increase in C_p is attributed to the short-range order structures and the formation of Cs_4Pb_4 clusters in the liquid [1,2]. These clusters significantly influence the thermodynamics of the melting transition, leading to the pronounced C_p peak. As the temperature increases beyond the melting point, their progressive dissociation leads to a continued decrease in C_p. This dissociation of the clusters can be observed in Fig. 4b where the species fractions have been calculated. The steep increase of the C_p above the melting point is related to the increase of the fraction of Pb^{-1} (of (Cs^{+1}) (Pb^{-1}) "cluster"). At higher temperature, after a maximum is reached, the fraction of Pb^{-1} decreases whereas those of Cs^{+1} and Pb increase, showing the decomposition of the clusters into pure Cs and Pb through the reaction (Cs^{+1}) (Pb^{-1}) = (Cs^{+1}) (Va) + (Cs^{+1}) (Pb). The model succeeds in capturing the ordering and the decomposition of the clusters at high temperature in the liquid. However, in our calculations, the predicted maximum of the heat capacity is lower than the values reported in Refs. [18,19] based on enthalpy measurements, and the subsequent decline at higher temperatures is less pronounced.

We also analyzed the composition dependence of the heat capacity of the liquid at 1000 K (Fig. 4c). As expected, the C_p is maximal at the equimolar composition $Cs_{0.5}Pb_{0.5}$ and decreases on both sides of this composition. A closer look at site fractions in C_p at 1000 K as a function of x(Pb) (Fig. 4d) further confirms this trend: Pb^{-1} species dominate at x (Pb) = 0.5, while pure Pb content increases with x (Pb) in the Pb rich region. In comparison, in the Cs-rich region, the Cs^{+1} fraction increases, confirming the central role of cluster decomposition in controlling the thermodynamic characteristics of the liquid. These results are strong indicators of the existence of short-range order structure in the liquid, particularly for the $Cs_{0.50}Pb_{0.50}$ composition, and underline the need to explicitly address the Cs-Pb interactions in thermodynamic models in order to accurately reproduce the complex behavior of the system. The ionic liquid model reproduces very well the significant excess of the heat capacity of the liquids over additive values. Experimental measurements of heat capacity for Cs_4Pb_9 and $CsPb_4$ remain necessary to improve the model.

6.3.4. *Enthalpy and entropy of mixing*

The enthalpy (ΔH_{mix}), entropy (ΔS_{mix}) and Gibbs energy (ΔG_{mix}) of mixing provide fundamental insight into the thermodynamic stability and indication for short-range ordering in the melt.

As shown in Fig. 5a, the mixing enthalpy of Cs_xPb_y liquid solution remains negative across the entire range of lead concentration highlighting the thermodynamic stability of the liquid towards the pure elements. At 1000 K, close to the melting temperature, the enthalpy of mixing shows a sharp minimum at x(Pb) = 0.5. This minimum reflects the presence of short-range order due to the formation of Cs_4Pb_4 Zintl-type clusters complexes, which strongly affects the thermodynamics of

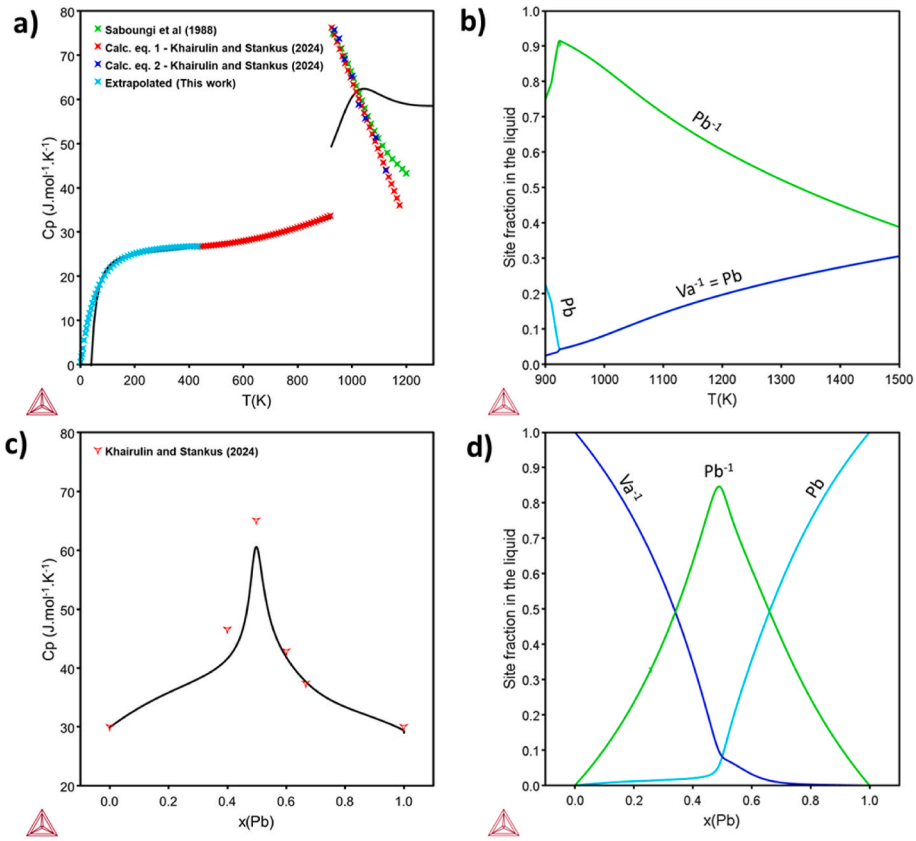


Fig. 4. a) Comparison of the calculated heat capacity (C_p) of $Cs_{0.5}Pb_{0.5}$ (black line) from the model in this study with previously reported data derived differentiation of the numerical fit of experimental enthalpy increment data, b) Calculated species site fractions in the liquid phase, c) Dependence of calculated C_p (black line) on composition at 1000 K as a function of Pb molar fraction, d) Calculated species site fraction at 1000 K as function of composition.

mixing by introducing significant non-ideal contributions, like for the heat capacity, indicating local organization within the liquid. As temperature increases, this ordering is gradually disturbed by cluster decomposition, leading to a less negative enthalpy of mixing, tending toward an ideal mixing at high temperature. The same tendency in the mixing enthalpy was found in the Na-Pb system [38].

The same ΔS_{mix} behaviour showing a sharp minimum at the equimolar position was detected for Rb-Pb and K-Pb in which short range ordering was observed in the liquid for the equimolar composition [39]. With increasing temperature, the mixing entropy increases. This is due to the clusters decomposition and the subsequent increase of the disorder (free Cs and Pb).

The phase diagrams for Cs-Pb, Rb-Pb and K-Pb [40] are very similar as well with the existence of a sharp liquidus curve at this equimolar composition. The resistivity measurements also show a sharp maximum at the equimolar composition, with a much higher magnitude for Cs-Pb compared to Rb-Pb and K-Pb. The trend of the excess contribution magnitude could be explained by the increase of ions size and polarizability: Na < K < Rb < Cs. This could explain both the much lower mixing enthalpy and entropy for Cs-Pb compared to the other alloys.

This behaviour is also consistent with the Cp curves for the three systems, which exhibit a sharp increase above the melting of the equimolar compounds and then a decrease at higher temperature, when the clusters decompose.

The entropy of mixing also shows a minimum at the same composition and temperature, consistent with the presence of Cs_4Pb_4 cluster. On the Cs-rich side, the entropy remains slightly positive as reported in the Rb-Pb system [39] and increases with temperature, whereas, in the Pb-rich side, it becomes significantly positive only at higher temperature (1500 K).

The Gibbs Energy of mixing also shows a minimum at x(Pb) = 0.5 further highlighting the presence of the local short ordering in the liquid associated with the formation of Cs_4Pb_4 clusters.

6.3.5. *Activity*

Fig. 6 illustrates the calculated natural logarithm of the activity of cesium (ln a(Cs)) as a function of the cesium mole fraction (x(Cs)) in the Pb rich liquid of the Cs-Pb system at various temperatures (T = 960 K, 1010 K, 1068 K, 1104 K) compared to the experimental data [25]. Overall, the calculated activities reproduce the experimental measurements satisfactorily. However, the modelled activity at 1104 K shows a slight overestimation of the corresponding measured value.

7. Conclusion

In this work, a comprehensive thermodynamic modelling of the Cs-Pb system was performed using the CALPHAD approach. This analysis incorporated a critical review of existing experimental data from the literature as well as DFT calculations. The DFT results show that the compounds CsPb and Cs_4Pb_9 and $CsPb_4$ are stable at low temperatures. The CALPHAD model reproduces very well the enthalpy of formation computed using DFT for these three compounds. The calculated phase boundaries generally agree reasonably well with the experimental data although invariant plateaus of phase transitions had to be reinterpreted using the compounds found stable in our study. New phase diagram measurements are necessary to check the phase diagram and decrease the uncertainties, especially between CsPb-$CsPb_4$. In this assessment, we optimized liquid thermodynamic parameters, using experimental enthalpy increment and activity data. The two-sublattice ionic liquid model was leveraged in this assessment to describe the short-range

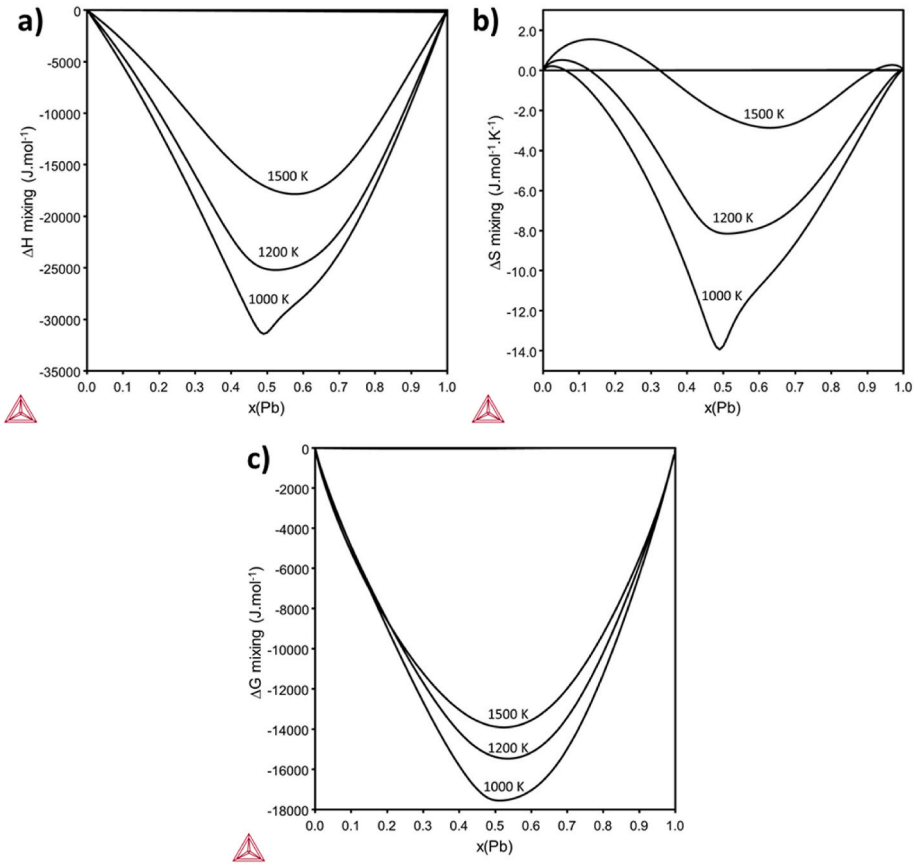


Fig. 5. Temperature dependence of calculated a) enthalpy, b) entropy and c) Gibbs energy of mixing as a function of x(Pb) for CsPb system in liquid phase. The gas phase was suspended in the calculation.

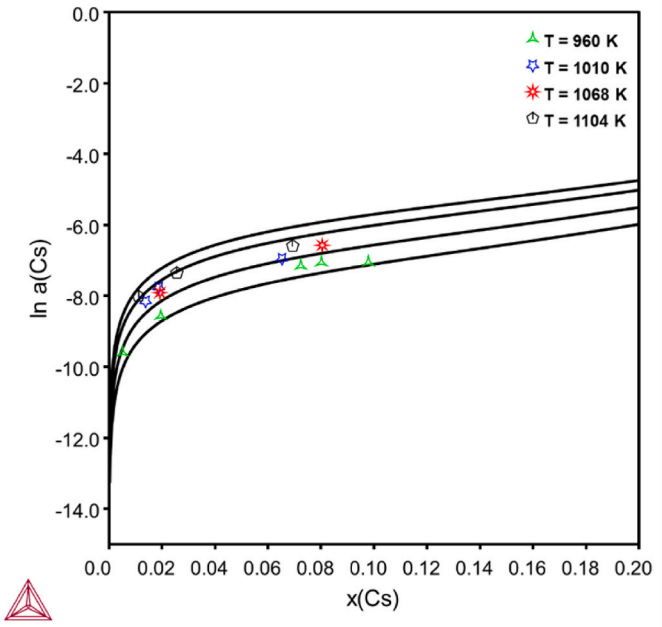


Fig. 6. Calculated activity of Cs in Cs-Pb system at various temperatures (T = 960 K, 1010 K, 1068 K, 1104 K) in comparison with experimental data [25]. The activity is referred to pure liquid Cs and Pb at the same temperatures.

ordering in the liquid, with the formation of Cs_4Pb_4 clusters followed by the decomposition of these clusters at high temperature. This work shows that the ionic liquid model is suitable to describe the short-range ordering and the speciation in the liquid phase. Further thermodynamic measurements of the compounds represented in the phase diagram (Cs_4Pb_9 and $CsPb_4$) are essential in order to verify and support the assessment. This first full thermodynamic model provides relevant phase behavior information, which is crucial for technologies such as nuclear reactors, where it is essential to understand material behavior at high temperatures. Likewise, the findings of this study will help optimize materials and processes used in solar energy-related applications, by extending this thermodynamic database with the introducing of I, Br and Sn to model (Cs) (Pb,Sn) $(Br,I)_3$ perovskites.

CRediT authorship contribution statement

Rania Zaier: Writing – original draft, Visualization, Validation, Methodology, Investigation, Formal analysis, Data curation, Conceptualization. **Andries van Hattem:** Writing – review & editing, Data curation. **Brandon N. de Waal:** Writing – review & editing, Data curation. **Rudy J.M. Konings:** Writing – review & editing, Validation, Formal analysis, Data curation. **Anna L. Smith:** Writing – review & editing, Data curation. **Philippe Zeller:** Writing – review & editing, Validation, Methodology, Formal analysis, Data curation, Conceptualization. **Christine Guéneau:** Writing – review & editing, Validation, Supervision, Methodology, Data curation, Conceptualization.

Declaration of competing interest

The authors declare no conflict of interest.

Appendix A. Supplementary data

Supplementary data to this article can be found online at https://doi.org/10.1016/j.calphad.2026.102941.

Annex 1. Parameters for the DFT calculations

Parameter		Step 1: structure search	Step 2: refinement	Step 3: Spin-Orbit Coupling
Exchange-correlation functional F_{xc}		PBESOL and PW91	RSCAN and R2SCAN	PBEsol
Pseudopotential library		2017R2 [28]	2017R2 [28]	SOC19 [32]
Plane-wave energy cutoff		318 eV	400 eV	800 eV
FFT grid scale		1.75	1.75	1.75
Augmentation density fine grid scale		2.1	5.25	5.25
Gaussian occupation function smearing width		0.07 eV	0.05 eV	0.05 eV
Brillouin zone sampling interval		0.05 $Å^{-1}$	0.025 $Å^{-1}$	0.025 $Å^{-1}$
SCF convergence threshold		2.0 10^{-6} eV/atom	5.0 10^{-8} eV/atom	5.0 10^{-8} eV/atom
BFGS convergence thresholds	Energy	5.0 10^{-5} eV/atom	5.0 10^{-6} eV/atom	5.0 10^{-6} eV/atom
	Force	0.1 eV/Å	0.02 eV/Å	0.02 eV/Å
	Stress	0.2 GPa	0.02 GPa	0.02 GPa
	Displacement	0.005 Å	0.001 Å	0.001 Å

Data availability

All the files are provided

References

[1] R.A. Khairulin, R.N. Abdullaev, S.V. Stankus, Volumetric properties of the liquid Cs-Pb system, Phys. Chem. Liq. 59 (2021) 162–168, https://doi.org/10.1080/00319104.2020.1793335.

[2] A.Sh Agazhanov, R.N. Abdullaev, S.V. Stankus, A.R. Khairulin, Thermal conductivity of the Cs-Pb system liquid alloys, Phys. Chem. Liq. 61 (2023) 253–263, https://doi.org/10.1080/00319104.2023.2207712.

[3] J. Zhang, G. Hodes, Z. Jin, S. Liu, All-inorganic CsPbX3 perovskite solar cells: progress and prospects, Angew. Chem. Int. Ed. 58 (2019) 15596–15618, https://doi.org/10.1002/anie.201901081.

[4] X. Li, Ye Wu, S. Zhang, Bo Cai, Yu Gu, J. Song, H. Zeng, CsPbX3 quantum dots for lighting and displays : Room-temperature synthesis, photoluminescence superiorities, underlying origins and white light-emitting diodes, adv. Funct. Mat. 26 (2016) 2435–2445, https://doi.org/10.1002/adfm.201600109.

[5] F. Cappia, B.D. Miller, J.A. Aguiar, L. He, D.J. Murray, B.J. Frickey, J.D. Stanek, J. M. Harp, Electron microscopy characterization of fast reactor MOX joint oxyde-gaine (JOG), J. Nucl. Mater. 531 (2020) 151964, https://doi.org/10.1016/j.jnucmat.2019.151964.

[6] S. Ohno, S. Miyahara, Y. Kurata, Test results of volatile radionuclide evaporation from liquid lead-bismuth and their comparison with test from sodium pool. Proceedings of 15th International Conference on Nuclear Engineering ICONE-15, 2007. Nagoya, Japan, April.

[7] M.M.R. Williams, D.G. Cacuci, Handbook of Nuclear Engineering, Springer, 2010, https://doi.org/10.1016/J.ANUCENE.2010.12.015.

[8] I. Trivedi, J. Sienickib, M. Bucknorb, K. Ivanova, Retention of radionuclides in heavy liquid metal coolants for mechanistic source term analysis, in: Proc. Int. Conf. on Mathematics and Computational Methods Applied to Nuclear Science and Engineering, Jeju, Republic of Korea, Apr. 16 2017.

[9] L. Duan, H. Zhang, M. Liu, M. Grätzel, J. Luo, Phase-pure γ-$CsPbI_3$ for efficient inorganic perovskite solar cells, ACS Energy Lett. 7 (2022) 2911–2918, https://doi.org/10.1021/acsenergylett.2c01219, 10.1021/acsenergylett.2c01219.

[10] X. Jia, C. Zuo, S. Tao, K. Sun, Y. Zhao, S. Yang, M. Cheng, M. Wang, Y. Yuan, J. Yang, F. Gao, G. Xing, Z. Wei, L. Zhang, H.-L. Yip, M. Liu, Q. Shen, L. Yin, L. Han, S. Liu, L. Wang, J. Luo, H. Tan, Z. Jin, L. Ding, CsPb(I Br1−)3 solar cells, Sci. Bull. 64 (2019) 1532–1539, https://doi.org/10.1016/j.scib.2019.08.017.

[11] M.I. Jamesh, H. Tong, M. Du, W. Niu, G. Jia, K.C. Cheng, C.W. Hsieh, H.H. Shen, B. Xu, Y. Tian, X. Xu, H.Y. Hsu, Advancement of technology towards developing perovskite-based solar cells for renewable energy harvesting and energy transformation applications, npj Mater. Sustain. 3 (2025) 29, https://doi.org/10.1038/s44296-025-00073-9.

[12] N. Pai, D. Angmo, Powering the future: opportunities and obstacles in lead-halide, inorganic perovskite solar cells, Adv. Sci. 12 (2025) 2412666, https://doi.org/10.1002/advs.202412666.

[13] S. Lee, S. Cho, S.H. Jeong, W. Lee, D. Pyun, J. Nam, J.S. Hwang, Y. Kim, Y. Kang, D. Kim, H.S. Lee, Inverted $CsPbI_3$ perovskite solar cells with all solution processed layers fabricated in high humidity, Commun. Mater. 6 (2025) 72, https://doi.org/10.1038/s43246-025-00796-1.

[14] J.A. Meijer, G.J.B. Vinke, W.V.D. Lugt, Resistivity of liquid Rb-Pb and Cs-Pb alloys, J. Phys. F Met. Phys. 16 (1986) 845–851, https://doi.org/10.1088/0305-4608/16/7/012.

[15] L.L. Zusman, Л.Л. ЗусМан, Diagram of the state of Pb–Cs alloys (ДиаграММа состояния сплавов Pb–Cs), in: L.L. Novikov, Л.Л. Новиков (Eds.), Physical, Mechanical and Thermal Properties of Metals (Фазовые Переходы В Металлах И Сплавах), Nauka (Наука), 1976, p. 105.

[16] M. Baitinger, K. Peters, M. Somer, W. Carrillo-Cabrera, Y. Grin, R. Kniep, Crystal structure of tetrarubidium telra/zetfro-tetraplumbide, Rb4Pb4 and of tetracaesium tetrahedro-telraplumbide, Cs4Pb4 214 (1999) 455–456, https://doi.org/10.1515/ncrs-1999-0427.

[17] E. Todorov, S.C. Sevov, Deltahedral clusters in neat solids: synthesis and structure of the zintl phase Cs_4 Pb_9 with discrete Pb_9^{4-} clusters, Inorg. Chem. 37 (1998) 3889–3891, https://doi.org/10.1021/ic980266v.

[18] M.-L. Saboungi, H.T.J. Reijers, M. Blander, G.K. Johnson, Heat capacity of some liquid zintl compounds: equiatomic alkali–lead alloys, J. Chem. Phys. 89 (1988) 5869–5875, https://doi.org/10.1063/1.455538.

[19] A.R. Khairulin, S.V. Stankus, Enthalpy and heat capacity of Cs–Pb alloys in solid and liquid states, Int. J. Thermophys. 45 (2024) 67, https://doi.org/10.1007/s10765-024-03362-y.

[20] A. Jain, S.P. Ong, G. Hautier, W. Chen, W.D. Richards, S. Dacek, S. Cholia, D. Gunter, D. Skinner, G. Ceder, K.A. Persson, Commentary: the materials project: a materials genome approach to accelerating materials innovation, APL Mater. 1 (2013) 011002, https://doi.org/10.1063/1.4812323.

[21] S. Kirklin, J.E. Saal, B. Meredig, A. Thompson, J.W. Doak, M. Aykol, S. Rühl, C. Wolverton, The open quantum materials database (OQMD): assessing the accuracy of DFT formation energies, npj Comput. Mater. 1 (2015) 15010. OQMD entry for CsPb. Available at: https://oqmd.org/materials/composition/CsPb.

[22] H.T.J. Reijers, M.-L. Saboungi, D.L. Price, J.W. Richardson, K.J. Volin, W. Van Der Lugt, Structural properties of liquid alkali-metal – lead alloys: NaPb, KPb, RbPb, and CsPb, Phys. Rev. B 40 (1989) 6018–6029, https://doi.org/10.1103/PhysRevB.40.6018.

[23] M. Hillert, B. Jansson, B. Sundman, J. Ågren, A two-sublattice model for molten solutions with different tendency for ionization, Metall. Trans. A 16 (1985) 261–266, https://doi.org/10.1007/BF02815307.

[24] T.P. Martin, Compound clusters. II. Intermetallics and phosphides, J. Chem. Phys. 83 (1985) 78–84, https://doi.org/10.1063/1.449795.

[25] L. Yamshchikov, S. Raspopin, V. Gusev, Thermodynamic characteristics of cesium in lead melts, Izv. Vysshikh Ucheb- Nykh Zaved. Chernaya Metall. (2001) 34–36.

[26] J.W. Furness, A.D. Kaplan, J. Ning, J.P. Perdew, J. Sun, Accurate and numerically efficient r^2 SCAN meta-generalized gradient approximation, J. Phys. Chem. Lett. 11 (2020) 8208–8215, https://doi.org/10.1021/acs.jpclett.0c02405.

[27] S.J. Clark, M.D. Segall, C.J. Pickard, P.J. Hasnip, M.I.J. Probert, K. Refson, M. C. Payne, First principles methods using CASTEP, Z. Kristallogr. Cryst. Mater. 220 (2005) 567–570, https://doi.org/10.1524/zkri.220.5.567.65075.

[28] BIOVIA, Dassault Systèmes, Materials Studio, Dassault Systèmes, San Diego, 2020 version 20.1.0.2728.

[29] J.P. Perdew, A. Ruzsinszky, G.I. Csonka, O.A. Vydrov, G.E. Scuseria, L. A. Constantin, X. Zhou, K. Burke, Restoring the density-gradient expansion for exchange in solids and surfaces, Phys. Rev. Lett. 100 (2008) 136406, https://doi.org/10.1103/PhysRevLett.100.136406.

[30] A.P. Bartók, J.R. Yates, Regularized SCAN functional, J. Chem. Phys. 150 (2019) 161101, https://doi.org/10.1063/1.5094646.

[31] B.G. Pfrommer, M. Côté, S.G. Louie, M.L. Cohen, Relaxation of crystals with the quasi-Newton method, J. Comput. Phys. 131 (1997) 233–240, https://doi.org/10.1006/jcph.1996.5612.

[32] CASTEP Developers. (n.d.). Overview: CASTEP pseudopotential library. CASTEP Docs. https://castep-docs.github.io/castep-docs/.

[33] Thermo-Calc Software, Version 2024b, Thermo-Calc Software AB, Stockholm, Sweden. Available at: https://www.thermocalc.com.

[34] A.T. Dinsdale, Sgte data for pure elements, Calphad 15 (1991) 317–425.
[35] Thermo-Calc Software, SSUB5: SGTE Substances Database, Version 5.2, Thermo-Calc Software AB, Stockholm, Sweden. Available at: https://www.thermocalc.com.
[36] O. Redlich, A.T. Kister, Algebraic representation of thermodynamic properties and the classification of solutions, Ind. Eng. Chem. 40 (1948) 345–348, https://doi.org/10.1021/ie50458a036.
[37] Thermo-Calc Software, PURE5: SGTE unary (Pure Elements) database, version 5.2, thermo-calc software AB, Stockholm, Sweden. Available at: https://www.thermocalc.com.
[38] S. Matsunaga, T. Ishiguro, S. Tamaki, Thermodynamic properties of liquid Na-Pb alloys, J. Phys. F Met. Phys. 13 (1983) 587, https://doi.org/10.1088/0305-4608/13/3/009.
[39] P.J. Tumidajski, A. Petric, T. Takenada, A.D. Pelton, M.-L. Saboungi, Thermodynamic properties of liquid Rb-Pb alloys, J. Phys. Condens. Matter 2 (1990) 209, https://doi.org/10.1088/0953-8984/2/1/017.
[40] J.S. Bookless, J.J. Egan, Use of F centers for the investigation of alloy thermodynamics. Potassium-lead system, J. Phys. Chem. 76 (1972) 1202–1205.